AIP | Physics of Fluids

Simulation and modeling of turbulence subjected to a period of uniform plane strain

Christopher J. Zusi and J. Blair Perot

Citation: Phys. Fluids **25**, 110819 (2013); doi: 10.1063/1.4821450
View online: http://dx.doi.org/10.1063/1.4821450
View Table of Contents: http://pof.aip.org/resource/1/PHFLE6/v25/i11
Published by the AIP Publishing LLC.

PHYSICS OF FLUIDS **25**, 110819 (2013)

Simulation and modeling of turbulence subjected to a period of uniform plane strain

Christopher J. Zusi and J. Blair Perot
Department of Mechanical and Industrial Engineering, University of Massachusetts Amherst, Amherst, Massachusetts 01003, USA

(Received 13 December 2012; accepted 26 August 2013;
published online 27 September 2013)

Direct numerical simulation is used to evaluate the effect of plane strain on isotropic homogeneous turbulence. The subsequent return to isotropy after the removal of the strain is also investigated. Large, moderate, and small strain rates are computed at moderate turbulence Reynolds numbers. The initial turbulence is generated via mechanical mixing so that the large scale turbulence develops relatively naturally. Turbulence length scales, Reynolds numbers, decay rates, and anisotropy are computed over the range of the simulations, with the goal of quantifying how anisotropic decay behaves. The simulations indicate that large scale anisotropy may not decay to zero at very large times. In agreement with experimental data, the presence of a recovery region is discerned before the return process is observed. Trajectory crossing is observed on the anisotropy invariant map indicating that anisotropy itself is not sufficient to determine its time evolution. Model constants for classic return-to-isotropy models are determined from the data and shown to vary with time. The oriented-eddy collision model [M. B. Martell and J. B. Perot, "The oriented-eddy collision turbulence model," Flow, Turbul. Combust. **89**(3), 335 (2012)], which includes turbulent structure information, is shown to predict the salient structure of the straining and return process. © *2013 AIP Publishing LLC*. [http://dx.doi.org/10.1063/1.4821450]

I. INTRODUCTION

Isotropic turbulence subjected to plane strain is a canonical case for investigating the fundamental properties of turbulence and for developing turbulence models. In the situation of plane strain, the mean velocity stretches the fluid in one direction while compressing it in another orthogonal direction at a rate that makes the mean flow incompressible. In this work, stretching occurs in the x direction while compression is in the y direction. The mean velocity during the strain is therefore, $u = Sx$ and $v = -Sy$, where S is a constant. This type of mean flow is found in 2D stagnation point flows. The classic example is the leading edge of a wing or turbine blade. The flow is interesting for this practical application but also because it is perhaps the simplest incompressible turbulent flow that involves a mean flow gradient. This turbulent flow is the next step up in complexity from decaying isotropic turbulence.

The decay of turbulence that has been subjected to plane strain is interesting because it is a case in which the turbulence is homogeneous but not isotropic. After the strain, the fluctuations have different magnitudes in the three different principal directions. The generation of anisotropy via constant plane strain can be precisely defined and therefore accurately reproduced in both experiments and in other numerical simulations. It is hypothesized that anisotropic turbulence tends to return to the isotropic state if no other influences are present. This return process is part and parcel of the energy cascade that transfers energy from large length-scale eddies to smaller length-scale eddies. Studying return-to-isotropy is therefore equivalent to studying the energy cascade for anisotropic turbulence. Since in practice, almost all turbulence is not isotropic, this is an important endeavor.

The return-to-isotropy process is difficult to accurately model. Most turbulence models assume that return-to-isotropy is solely a function of the degree of anisotropy of the velocity fluctuations.

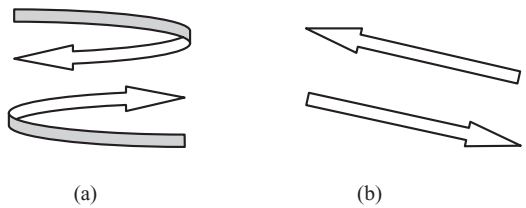

FIG. 1. (a) Pancake shaped eddies typical of many stratified turbulent flows and (b) long jet like eddies common in shear flow.

However, one primary observation of this paper is that velocity fluctuation anisotropy, in itself, is not sufficient to predict the-return-to-isotropy rates. The idea that more information than Reynolds stress anisotropy is needed to predict anisotropic decay is not new. It has been present by Kassinos and Reynolds[2–5] and their co-workers. In addition, perhaps, the earliest references to the basic idea can be attributed to the turbulence research group at Los Alamos.[6,7]

The argument that Reynolds stress anisotropy is not sufficient to predict anisotropic turbulence decay (developed by these prior groups) is as follows. Two turbulent flows can have identical Reynolds stress tensors, and therefore identical anisotropy tensors, and yet be very different. For example, turbulence stratified by density or rotation (as in the atmosphere or ocean) has pancake shaped eddies that are "flat" in one direction (normal to gravity in the density stratified case). In contrast, the turbulence generated by a shear flow tends to be elongated in one direction (cigar shaped) (see Figure 1). Despite clear differences in their structure, both flows can have identical Reynolds stress tensors and anisotropy tensors. This suggests that the fluctuations alone (the anisotropy tensor) do not provide enough information about the turbulence to accurately predict the tensor's evolution. Reynolds and Kassinos define additional single-point tensor quantities based on the streamfunction derivatives that contain additional information about the dimension, "circulicity," and "stropholysis" of the turbulence. In contrast, Harlow and co-workers use information from the two-point correlations to provide the additional information required to predict anisotropic decay and return-to-isotropy.

In this paper, we will explore the use of two-point structure information similar to the Harlow group (though developed without knowledge of that work) rather than one-point statistics of the streamfunction derivatives (as done in the works of Kassinos, Reynolds, and co-workers) as the additional information necessary to close the system. For rapid distortion theory (RDT) these two approaches are equivalent, as they must be. But for the decay case (which is the antithesis of RDT) it is no longer clear that both approaches to understanding and modeling the anisotropic decay process are still equivalent.

Experiments of plane strain and the return to isotropy have a long history dating from the experiments of Townsend[8] in 1954 that used a 4:1 straining ratio. These experiments were followed by those of Tucker and Reynolds[9,10] who used a higher straining ratio (6:1). Over a decade later, Gence and Mathieu[11] performed further experiments of plane strain and its subsequent return to isotropy. Le Penven *et al.*[12] performed two experiments, one of which was close to plane strain in order to show that the simple Rotta model[13] for return-to-isotropy was inadequate. Choi and Lumley[14] and Lumley and Newman[15] used these prior experiments as well as their own to propose models for return-to-isotropy.

Perhaps the first numerical simulations of plane strain were performed by Kwak[16] in his Ph.D. thesis completed in 1975. Those simulations, at 16^3 and 32^3 mesh resolutions, were soon replaced by larger calculations using 128^3 meshes. For example, Rogallo[17] in 1981 demonstrated the moving mesh numerical approach that will also be used in this work (though with a very different numerical method). Then in 1985, Lee and Reynolds[18] performed 128^3 simulations for a variety of different strain configurations that are still used widely today. Lee and Reynolds suggested that small scale anisotropy relaxes rapidly initially but then relaxes with the large-scale anisotropy over longer time scales. Rogers and Moin[19] looked at the instantaneous flow structures in those configurations. Recently Barre *et al.*[20] have performed 96^3 direct numerical simulations (DNS) of particle laded turbulent plane strain.

Kevlahan and Hunt[21] discuss the theory for turbulence when it is being strained. Under very large strains, RDT[22] applies. The turbulence evolution can be linearized and solved exactly in this limit. Hällback *et al.*[23] describe how this linear theory can even be applied to the nonlinear cascade related terms like the dissipation rate tensor. RDT proves that Reynolds stresses alone contain insufficient information to predict their own evolution when the turbulence is subjected to large strain. This work hypothesizes (like Reynolds and Kassinos, and Harlow, before us) that the additional structural information necessary to predict turbulence evolution under the influence of rapid strain (RDT) remains important even after that strain is removed.

This work follows the strategy of Moin who has long advocated the use of direct numerical simulation to investigate the fundamental physics of turbulent flows.[24] In particular, it is the logical successor to the pressure-strain investigations of Perot and Moin[25,26] on the return-to-isotropy process near walls.

There is little in the way of theory that applies directly to the decay of anisotropic turbulence, but isotropic decay has been very extensively studied. A review of isotropic decay theory can be found in Perot.[27] One of the most critical results for isotropic decay is due to Saffman[28] and it shows that the behavior of the large scale correlations (or small wave numbers) dictates the decay rate. This means that both experiments and simulations must be careful to keep the large eddy length-scale much smaller than the tunnel size or simulation domain. Reference 27 shows that $L = \frac{K^{3/2}}{\varepsilon}$ should be less than 1/4 of the periodic domain size or the decay of isotropic turbulence becomes length-scale constrained. In order to capture both the large and the small scales, the simulations reported in this work will be at resolutions of 512^3. The details of the numerical simulation are presented in Sec. II. The additional resolution in the simulations is not used to increase the turbulent Reynolds numbers over prior plane-strain calculations. It is used to capture the influential large scales better and to produce smoother statistics. The simulations in this work are similar in Reynolds number and resolution to the well resolved simulations of de Bruyn Kops and Riley.[29] The turbulent Reynolds numbers present in these simulations should be sufficient to capture the fundamental physics. The turbulent Reynolds number in the majority of the cases simulated is nearly the same as the turbulent Reynolds numbers in the classic decay experiments of Comte-Bellot and Corrsin.[30]

Another important aspect of the simulations presented in this work relates to the generation of the initial isotropic turbulence. It is well understood that the small wavenumbers (or large correlation scales) are set by the initial conditions and are invariant during the decay process. Most simulations therefore inadvertently impose the decay behavior via the choice of the initial turbulence spectrum or initial turbulence forcing. It is desired for these studies that the large scale correlations be formed physically, and not via the specification of initial conditions. The initial flow for these simulations is therefore a velocity and pressure of zero. The turbulence is then generated physically by having small solid and stationary "mixing boxes" in the domain (768 of them for the 512^3 simulations) (see Figure 2). The fluid is driven past these boxes with a randomly time varying but spatially uniform pressure gradient. After the turbulence is established (developing all the long range correlations

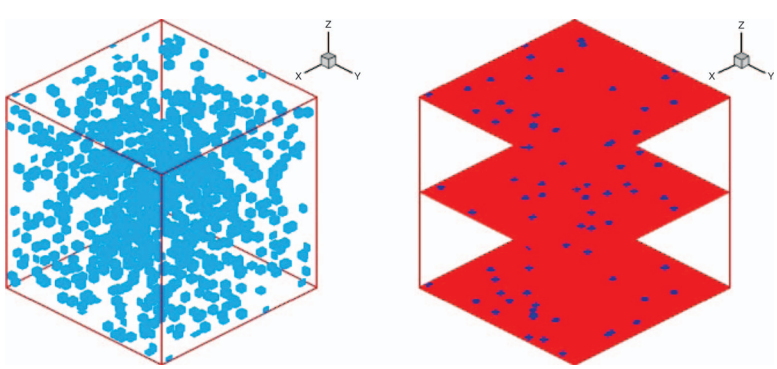

FIG. 2. On the left, stationary mixing cubes located in the simulation domain. On the right, 2D slices in the XY-plane help to better show the mixing cube density.

naturally), the boxes "melt" and become zero velocity fluid. More detail on the turbulence generation process is provided in Sec. II and in Ref. 27.

Wind tunnel experiments have some problems producing truly isotropic initial conditions. Kurian and Fransson[31] show that the use of a contraction to isotropize the Reynolds stresses that result from the anisotropic wind tunnel grid turbulence does not also isotropize the two-point correlations. It is suspected that this underlying anisotropy in the turbulence structure has some effect on both the strained turbulence and the subsequent return-to-isotropy.

Numerical simulation allows this investigation to observe the turbulence over very long times and at high temporal resolution. Some of the quantities that will be of interest, such as the decay rate, are extremely sensitive and require both high temporal resolution and long times to accurately calculate. The turbulence statistics before, during, and after the straining are examined in Sec. III. The modeling of the strain and return-to-isotropy process is described in Sec. IV, and a discussion of the results is presented in Sec. V.

II. SIMULATION METHODOLOGY

A. Numerical method

The incompressible Navier-Stokes equations with constant viscosity are solved with the classic 2nd-order Cartesian staggered mesh spatial discretization of Harlow and Welch.[32] A 3-step and 2nd-order low-storage Runge-Kutta method is used for time advancement. The pressure and incompressibility constraint are enforced by using the classic fractional step method[33] or the exact projection method.[34] The inviscid, no penetration, boundary condition is directly enforced on walls with this discretization because the normal velocity flux on a wall is a primary unknown of the method. The viscous no-slip condition on walls is enforced by choosing velocity gradients on the wall so that the tangential velocity goes to zero on the wall.

This numerical discretization has been widely used for turbulence simulations when complex wall boundary conditions are present (see Perot and Moin,[25] Le and Moin,[35] Martell *et al.*,[36] and the references therein). This method is favored because it not only conserves mass and momentum like finite volume and spectral methods but because it also conserves physically important secondary variables such as vorticity and kinetic energy. The kinetic energy cascade is central to the correct physical prediction by any DNS simulation, so it is attractive to know that this discrete system respects the energy and vorticity physics of the Navier-Stokes equation system. The method is validated in Sec. II C. Numerical methods with attractive secondary conservation properties are discussed extensively in Perot,[37] and a general methodology for generating such discretizations can be found in Perot and Subramanian.[38]

Fourier spectral methods are common in DNS simulations of turbulence, and were used for all the previously cited simulations of plane-strain turbulence. However, in the situation where turbulence arises physically from mechanical stirring and it is not imposed as an *ad hoc* initial condition or due to a forcing term, Fourier spectral methods are not appropriate. The required wall boundary conditions cannot be imposed with an inherently periodic Fourier spectral method. The reader should be cautioned about assuming that Fourier methods are significantly more accurate than mimetic 2nd-order methods for DNS simulations. In DNS, the smallest scales are just barely resolved. As a result it is incorrect to assume that only the leading-order error term of a Taylor series expansion (or the order of accuracy) is the relevant measure of accuracy. The numerical method used in this work is kinetic energy, vorticity, mass, and momentum conserving and resolves the energy cascade and small scale fluctuations (dissipation spectra) at least as well as FFT based methods with the same resolution (see Sec. II C).

B. Turbulence generation

The generation of the turbulence is a relatively important component of this work because the large scale correlations have a direct affect on the decay process. It is therefore important that those large scales arise from some physical process (such as mixing by cubes) and are not being

directly imposed by any human choices about the initial conditions or the large scale forcing. For the simulations shown in this work 768 small no-slip cubes are randomly distributed throughout the domain (for the 512^3 cases). These small mixing cubes fill less than 2% of the total fluid volume (see Figure 1).

The cubes remain fixed in place and the turbulence is generated by imposing an external, constant in space, acceleration. This is equivalent to performing the calculation in a time varying linearly accelerating reference frame (shaking). The direction of this acceleration is changed randomly every 0.3 s, but its magnitude is specified by the user. The shaking time scale is much less than the initial large eddy timescale (which is of the order of 2.0), but long enough to create a wake behind each cube that is sufficiently long enough to interact on average with a neighboring cube. A typical value of the acceleration is 100 cm/s^2 (or about 1/10 the acceleration of gravity). The shaking is performed for 5.1 s in most simulations (or 17 different accelerations). The primary acceleration (shaking) is then turned off and a restoring acceleration, $\mathbf{a}_{return}$, is allowed to act for another 1.9 s. After 1.9 s the restoring acceleration (which is exponentially decaying in time) causes the mean flow to be extremely close to zero. A mean flow of zero is not necessary for the code, but it does allow the simulation to take slightly larger timesteps (by minimizing the Courant–Friedrichs–Lewy condition (CFL) stability criteria), and it does seem to lead to better statistical accuracy at very long times when the fluctuations can become smaller than the mean flow. During this 1.9 s period the turbulence changes from being accelerated to being in isotropic decay. At the end of this period (at a time of 7) the boxes instantaneously turn into zero velocity fluid. It tends to take about one or two large-eddy turnover times for the surrounding turbulence to fully merge with (chew up) the small regions of zero velocity fluid where the stirring boxes used to be. The flow tends to behave like ideal (Saffman, k^2) decaying turbulence by a time of 12.

Physical units are not needed by the computer, but can be helpful for the reader, and make the discussion simpler. If the simulated fluid is water at standard temperature and pressure (with $\nu = 10^{-2}$ cm^2/s) then the domain size (after straining) is a cube that is 48 cm on a side. The small cubes that stir the turbulence are 1.4 cm on a side. And in the 512^3 simulations there are 768 of them randomly placed in the domain. The total volume of all the stirring elements is therefore 1.93% of the total simulation volume. The mesh size itself is 0.9375 mm (which is 1/15th of the stirring cube size). At early times in the simulation, the timestep can be as small as 1/1000th of a second. In all the simulations it is never larger than a 1/10th of a second. All the simulations run out to a time of roughly 120 s. More details can be found in Ref. 27.

C. Validation

The 3D energy spectra and dissipation spectra are shown in Figures 3(a) and 3(b) at a time of 12 s (with solid black lines) for initial condition 2 (see Table I below). This is 5 s after the stirring boxes have been removed and the point at which the kinetic energy decay exponent asymptotes to its theoretical value of 6/5. These spectra are compared with other simulations and experiments. Symbols are data from the second measurement station of Comte-Bellot and Corrsin[30] (tU/M = 98). Dashed lines are the data from a simulation by Wray.[39] The experiments of Comte-Bellot and Corrsin have a Taylor microscale Reynolds number of 65.3 at this measurement station. The current simulations have a Taylor microscale Reynolds number of 50.8 at a time of 12 s.

The peaks of the present simulations and the Wray data have been scaled to match the peak in the experimental data. The wavenumbers were scaled to have the same large eddy length scale $L = \frac{K^{3/2}}{\varepsilon}$. Both the low wavenumber and high wavenumber (dissipation spectra) are well captured. de Bruyn Kops and Riley[29] also computed this Reynolds number with a spectral code and 512^3 mesh points, with very similar results.

D. Moving mesh for straining

When the fluid is being strained, the simulations are performed on a moving mesh that moves with the mean flow. The incompressible Navier-Stokes equations in an arbitrary moving reference

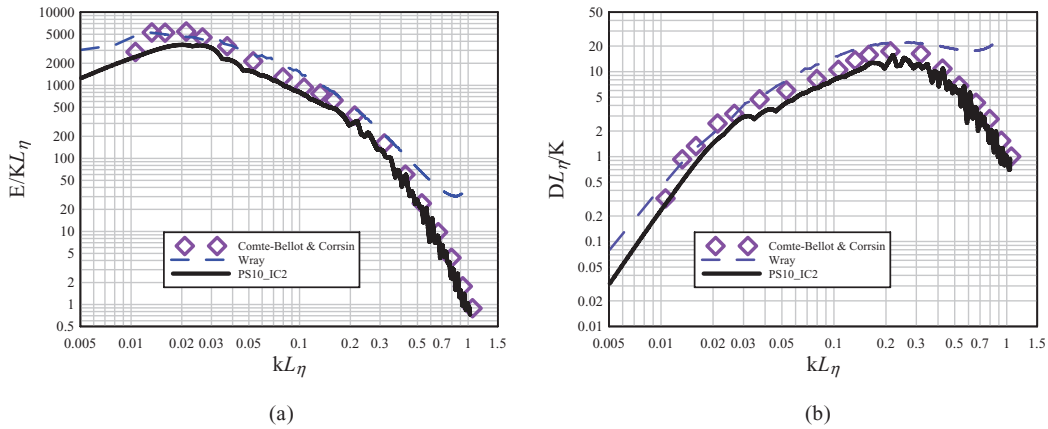

FIG. 3. (a) 3D energy spectra and (b) dissipation spectra. Solid lines (black) are the current simulations. Symbols are from Comte-Bellot and Corrsin[30] at tU/M = 98 (second station). Dashed lines (blue) are from a spectral 512^3 simulation performed by Wray.[39]

frame, moving with a velocity **v**, are

$$\frac{\partial \mathbf{u}}{\partial t} + (\mathbf{u} - \mathbf{v}) \cdot \nabla \mathbf{u} = -\nabla p + \nu \nabla^2 \mathbf{u}. \tag{1}$$

The equation for the mean velocity, which for the case of plane strain is constant in time and varies linearly in space, then becomes

$$(\bar{\mathbf{u}} - \mathbf{v}) \cdot \nabla \bar{\mathbf{u}} + \nabla \cdot (\overline{\mathbf{u}'\mathbf{u}'}) = -\nabla \bar{p}. \tag{2}$$

The second term is zero for plane strain where the turbulence is homogeneous, and for these simulations the reference frame moves with the mean flow ($\mathbf{v} = \bar{\mathbf{u}}$), so the first term is also zero. This means that the mean pressure is spatially constant (and set to zero for simplicity). As a result of Eq. (2), the equation for the fluctuating velocity, u'_i, in a moving frame is (in Cartesian tensor notation)

$$\frac{\partial u'_i}{\partial t} + u'_j u'_{i,j} + u'_j \bar{u}_{i,j} = -p'_{,i} + \nu \nabla^2 u'_i. \tag{3}$$

This has a form similar to the Navier-Stokes equations but with an extra source term (third term on the left hand side) that is due to the mean flow. For plane strain the mean velocity gradient tensor is a diagonal tensor and the result of this extra term is to cause exponential decay for the x-direction fluctuations and exponential growth of the y-direction fluctuations. Incompressibility, diffusion, and advection then modify this forcing term. In the RDT limit, the mean gradient forcing term is large and only the pressure is large enough to modify its effects.

Equation (3) is the Navier-Stokes equations in a reference frame moving with the mean flow. This idea was also used by Rogallo[17] in his FFT simulations of strained turbulence. Solution for the fluctuations rather than the total velocity is attractive because it allows one to use periodic boundary conditions for the sides of the simulation domain. In plane strain the total flow is not periodic because the mean flow is not periodic, but the fluctuating velocity and pressure fields can be represented as periodic fields.

In the simulations performed for this work the initial domain in which the stirring boxes reside and in which the turbulence is initially generated is shorter in the x-direction and is given by $L_x^{initial} = L_z e^{-ST}$, where T is the total straining time. Similarly, the initial domain is longer in the y-direction and is given by $L_y^{initial} = L_z e^{+ST}$. The domain (and mesh size L_z) in the z-direction remains fixed. The initial domain and mesh is shown in Figure 4(a). As the turbulence is strained the domain grows in the x direction and shrinks in the y direction (Figure 4(b)). Finally, at the end of the straining period the domain is perfectly cubic (Figure 4(c)). Different strain rates can be used with the same initially distorted mesh. What must remain constant is the product of strain rate, S, and the duration of the strain, T. For the computed plane strain cases in this work, $ST = 0.5$ with

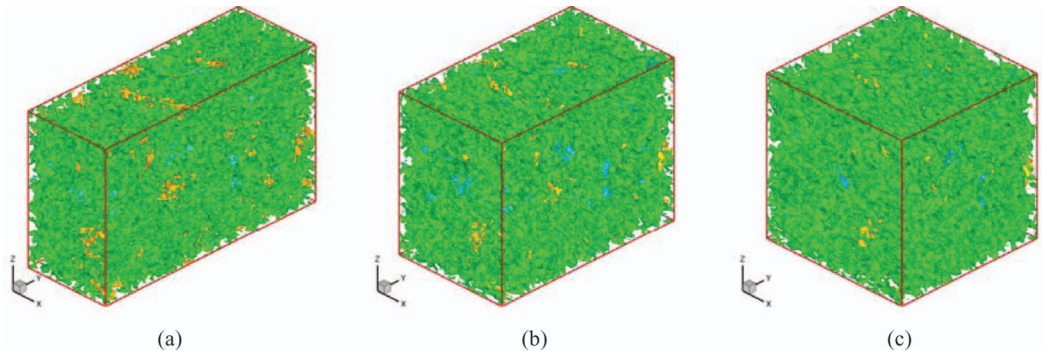

FIG. 4. Domain evolution during straining. (a) Domain at time 12.0 s before straining begins. (b) Domain at $ST = 0.25$, halfway through the straining process. (c) Final cubic domain after straining is complete (at $ST = 0.5$).

all straining starting at time = 12 s. A strain $S = 0.625\ \mathrm{s}^{-1}$, strains until 12.8 s ($ST = 0.5$), $S = 0.3125\ \mathrm{s}^{-1}$ strains until 13.6 s, $S = 0.15625\ \mathrm{s}^{-1}$ until 15.2 s, $S = 0.0625\ \mathrm{s}^{-1}$ until 20 s, and the case with $S = 0.025\ \mathrm{s}^{-1}$ strains until 32.0 s. After the domain becomes cubic in shape the strain is turned off. The resulting anisotropic turbulence now decays without strain, and with no more motion of the underlying mesh.

III. RESULTS

A. Initial conditions

A number of plane strain cases were run to investigate the effects of non-dimensional strain rate. Different initial conditions produce slightly different values for k and ε. Approximate values for the initial Sk_0/ε_0 (at time = 12) are ≈0.35, 0.865, 1.73, and 3.46. The largest dimensionless strain rate will be shown to approximate the theory of RDT well. These plane strain cases were also investigated across three different initial conditions (IC1, IC2, and IC3). The different initial conditions are generated by having a different random placement for the stirring boxes, and by shaking in different random directions (though at the same amplitude). Table I describes the properties of the three different initial conditions (at time = 12). In total there are 12 simulations involving 3 initial conditions and 4 strain rates, all at roughly the same initial turbulent Reynolds number.

TABLE I. Initial conditions for the three test cases at a time = 12 seconds (when straining begins).

	k_0	ε_0	Re_0	$Re_{\lambda 0}$	$T_0 = k_0/\varepsilon_0$	$L_0 = k_0^{3/2}/\varepsilon_0$	Sk_0/ε_0	L_η	$L_\eta/\Delta X$
IC1	0.848	0.151	477.466	56.419	5.628	5.184	Low = 0.352 Medium-low = 0.879 Medium-high = 1.759 High = 3.518	0.051	0.541
IC2	0.700	0.126	387.370	50.818	5.536	4.631	Low = 0.346 Medium-low = 0.865 Medium-high = 1.730 High = 3.460	0.053	0.566
IC3	0.534	0.099	287.880	43.809	5.396	3.941	Low = 0.337 Medium-low = 0.843 Medium-high = 1.686 High = 3.372	0.056	0.602

Table I shows the initial kinetic energy K_0, dissipation $\varepsilon_0 = -dk/dt$, and turbulent Reynolds number $Re_0 = \frac{K^2}{\nu\varepsilon}$. It also shows the Taylor micro-scale Reynolds number $Re_{\lambda 0} = (\frac{20}{3} Re_0)^{1/2}$, large-eddy turnover time $T_0 = K/\varepsilon$, large-eddy length scale $L_0 = \frac{K^{3/2}}{\varepsilon}$, and the Kolmogorov length scale $L_\eta = \nu^{3/4}/\varepsilon^{1/4}$. A grid spacing ΔX that is twice the Kolmogorov length scale or smaller is considered by most DNS practitioners to be more than sufficient for resolving small scales.

B. Time development

The behavior of the turbulent Reynolds number and the large-eddy length scale are shown as a function of time in Figure 5. This figure shows the behavior for three different initial conditions at the moderate strain rate (initial $Sk_0/\varepsilon_0 = 1.76$, 1.73, and 1.69). Other strain-rate cases behave similarly. Note that the length-scales (increasing set of blue lines) grow rapidly during the straining process (time 12–13.6) and the Reynolds number (decreasing set of green lines) also grows slightly during the straining as energy is added to the turbulence via the mean flow gradients. At a time of roughly 100 the turbulence is becoming box constrained. The IC1 case (solid blue line) exhibits the most abrupt transition to a fixed length-scale limit. In isotropic decaying simulations a length-scale of 10–12 is also found as the upper limit possible for the large-eddy length scale.[27] In what follows, results at times greater than 80 will be assumed to be influenced by the domain size of the simulation.

The Reynolds stresses for $Sk_0/\varepsilon_0 = 1.76$ and IC2 are shown in Figure 6 as they evolve in time. Again this case is indicative of the other strain rates and initial conditions. The Reynolds stresses

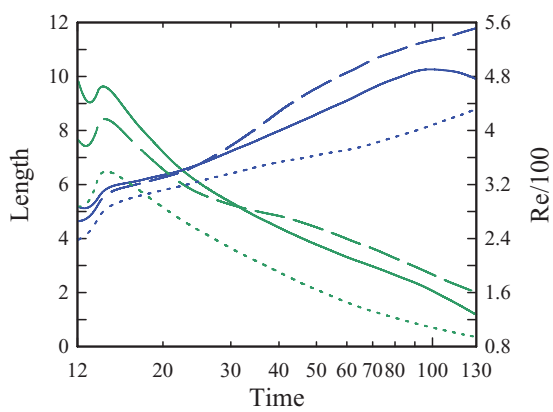

FIG. 5. Large eddy length scale (blue: left y-axis, increasing curves) and turbulent Reynolds number divided by 100 (green: right y-axis, decreasing curves) as a function of time for $Sk_0/\varepsilon_0 = 1.76$ for all three initial conditions. IC1 is solid line, IC2 is dashed line, and IC3 is dotted line.

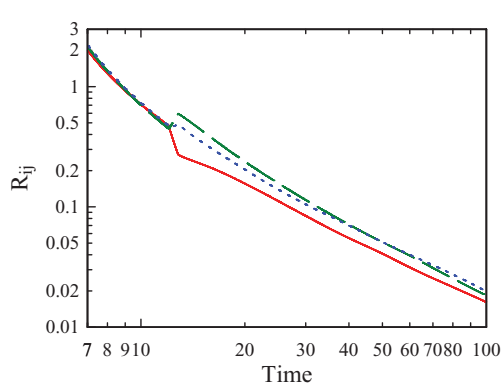

FIG. 6. Reynolds stresses for IC2 (with $Sk_0/\varepsilon_0 = 1.76$) as a function of time. R_{11}, solid red line; R_{22}, dashed green line; and R_{33}, dotted blue line.

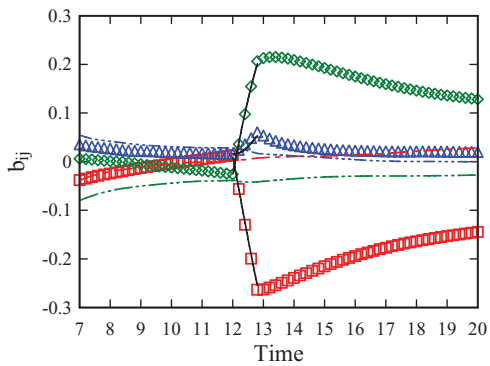

FIG. 7. Anisotropy tensor, b_{ij} resulting from IC2 subjected to $Sk_0/\varepsilon_0 = 3.46$. Strain runs from t = 12 to t = 12.8. b_{11}, red squares; b_{22}, green diamonds; and b_{33}, blue triangles. b_{12} (red, dashed-dotted line), b_{23} (green, dashed-dotted-dotted line), and b_{13} (blue, dashed-dotted-dotted-dotted line). RDT predictions are shown (black solid lines) from t = 12 to t = 12.8. There are 50 timesteps between each symbol in the figure.

decay with time, with an increase in R_{22} during the straining period and a more rapid decrease in R_{11}. In theory the off-diagonal components of the Reynolds stress tensor should be zero for this flow so the off-diagonal components are not shown here. They are shown in Figure 7 below and are small.

In this work, the dimensionless Reynolds stress anisotropy tensor is given by the expression $b_{ij} = \frac{\langle u_i u_j \rangle}{K} - \frac{2}{3}\delta_{ij}$ (other authors may use a similar definition that is 2 times smaller). This quantity removes the effect of the strong decay that dominates Figure 6, and allows one to focus on the deviations of the Reynolds stresses from the isotropic case. Figure 7 shows the anisotropy tensor corresponding to the same case as Figure 6. For statistical reasons the off-diagonal components of the anisotropy tensor are not zero. They are shown here (as lines without symbols) to give an indication of the statistical variability present in the results. A dimensionless anisotropy below 0.05 is therefore essentially statistically equivalent to zero in our results.

Figure 7 confirms the theoretically expected behavior of turbulence subjected to plane strain. For extension in the x-direction the b_{11} component of the tensor (red squares) decreases and becomes negative. The turbulence fluctuations in the x-direction are suppressed. Similarly, compression in the y-direction causes the b_{22} component of the anisotropy tensor (green diamonds) to increase. Fluctuations are amplified in the compression direction. The z-direction (blue triangles) is only indirectly affected by the strain. The turbulent fluctuations increase slightly in this direction as the energy reorients due to mixing from the y-direction. Figure 7 also shows the RDT prediction (which assumes very large dimensionless strain) for this case (solid, black lines) for the time 12–12.8. The DNS agreement with the RDT prediction is very good for this highest strain-rate case (the RDT lines lie right on top of the DNS data).

C. Strain rate

The influence of the strain rate on the anisotropy tensor is shown in Figure 8. This shows four different strain rates applied to the same initial condition (IC2). Keep in mind that each case uses a different strain rate. However, the total amount of strain in each case is the same so that the strain rate multiplied by duration of strain remains a constant (ST = 0.5). This means that the smaller the strain rate the longer it lasts.

To first order the curves are very similar after the straining is completed (their peak values and the end of the straining process are reasonably close). This confirms that the total strain and not the strain rate is the critical factor governing how much anisotropy is generated in the turbulence. Another important observation that we will return to later is the fact that immediately after the strain

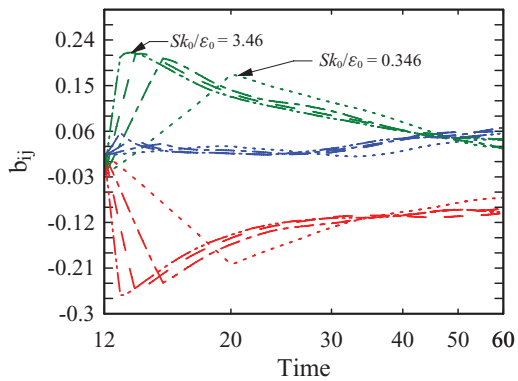

FIG. 8. Diagonal components of the anisotropy tensor during strain and subsequent decay (return to isotropy). Red lower curves, b_{11}; green upper curves, b_{22}; and central blue, b_{33}. Strain rates of $Sk_0/\varepsilon_0 = 0.346$, 0.865, 1.73, and 3.46 for initial conditions IC2.

is removed, the b_{11} and b_{33} components begin to return to isotropy, but the large b_{22} component (green) goes *away* from isotropy for some time (1–2 s) before finally beginning to decrease. This affect has been noticed in some experiments previously[40] and is also discussed in Refs. 3 and 4. We will refer to this period after the strain is removed, but before all components begin to reduce their isotropy, as the *recovery* period. It is hypothesized in this work that in this recovery period, the structures of the turbulence (the two-point correlation lengths) are returning to isotropy faster than the velocity fluctuations are returning. Once the structures (two-point lengths) rapidly recover their isotropic values the more classic mixing of eddies and return-to-isotropy of the velocity fluctuations takes over which we refer to as *return*.

At very long times, the anisotropy curves do not appear to asymptote to zero. They seem to asymptote to a fixed (non-zero) value. This could be a statistical effect, caused by the very largest eddies (the only ones left after very long times) not having enough statistical sample in the finite simulation domain. Experiments show similar results.[9,12]

Figure 9 shows the effect of having different initial conditions and roughly the same strain rate ($Sk_0/\varepsilon_0 = 3.52$ for IC1, $Sk_0/\varepsilon_0 = 3.46$ for IC2, and $Sk_0/\varepsilon_0 = 3.37$ for IC3). This figure confirms that the trends described above (particularly the recovery region) are general and not a result of one particular initial condition.

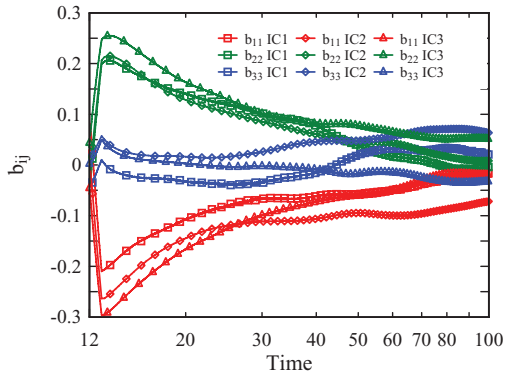

FIG. 9. Effect of initial conditions IC1, IC2, and IC3 at $Sk_0/\varepsilon_0 = 3.46$. This shows the statistical variation due to different realizations. Statistical anisotropy variation of the order of 0.05 is common.

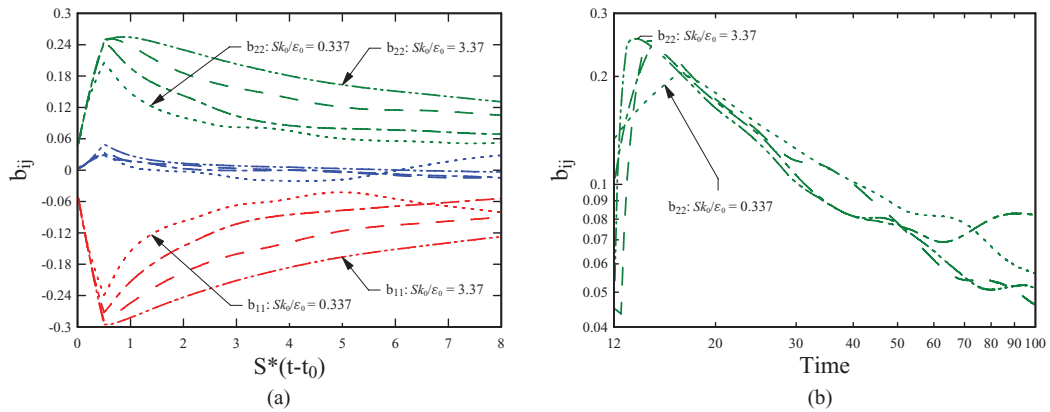

FIG. 10. Component of anisotropy tensor during strain and recovery of IC3 subjected to different strain rates. (a) b_{11}, b_{22}, and b_{33} of the anisotropy tensor with time axis scaled as $S^*(t - t_0)$. (b) log-log plot of b_{11} when each curve has been translated on the x-axis such that the point in time at which straining is stopped coincides with a point on the $Sk_0/\varepsilon_0 = 3.46$ trajectory.

D. Scaling

Two different scalings of the time axis are shown in Figure 10. The first scaling shown in Figure 10(a) uses a dimensionless timescale based on the strain rate, $t^* = S(t - 12)$. Under this scaling all the curves travel along the same lines during the straining process. The only difference is that the lower strain rates progress less far along those lines. Only the very lowest strain rate ($Sk_0/\varepsilon_0 = 0.35$) shows a noticeable difference. For this low strain rate, the return to isotropy mechanism is strong enough to slow the straining trajectory as it moves away from isotropy.

To obtain a collapse of the curves after the strain, a different scaling must be used (since there is no imposed external timescale anymore). The scaling used in Figure 10(b) simply shifts each curve to the left (in time) until its peak value (at the end of the strain) lies on the highest strain curve. This is essentially just a reset of the zero time to be the point at which strain ends. Interestingly, the subsequent evolution of the anisotropy behaves very similarly (the curves lie almost on top of each other). The linear behavior on the log-log plot indicates a power law decay.

E. Invariant map

The anisotropy invariant plot[41] is a common way to look at the return-to-isotropy problem. The anisotropy tensor has zero trace, so one can plot the state of the turbulence as a function of the other two invariants $II = -(1/8)b_{ij}b_{ji}$, and $III = (1/24)b_{ij}b_{jk}b_{ki}$. Figure 11 shows the variation of this turbulence state as a function of time for all three initial conditions and two different strain rates.

The turbulence starts close to the origin (isotropy) at time 12. The solid red lines show the evolution as the turbulence is strained and moves away from isotropy. When the strain is removed on the high strain case (Figure 11(a)) the state moves to the right on the invariant map. This is the recovery period and does not represent a significant return to isotropy. After some time the recovery (motion to the right) stops, and the state moves downward towards the isotropic state. At very long times, the trajectory wanders about near zero but no longer continues to approach it. We believe this is a result of the statistical sensitivity and domain constraint at large times. The three different initial conditions have somewhat different trajectories on the invariant map, but these general characteristics remain true for all of them.

The low strain case (Figure 11(b)) has the same general structure of strain (solid) line moving away from isotropy, and no strain (symbols) moving back towards isotropy. However, for the low strain case, return is almost back along the upward straining trajectory. There is far less recovery, or movement of the trajectory to the right. It is hypothesized that when the strain is weaker the structure of the turbulence (two-point correlation lengths) can remain more isotropic even as the

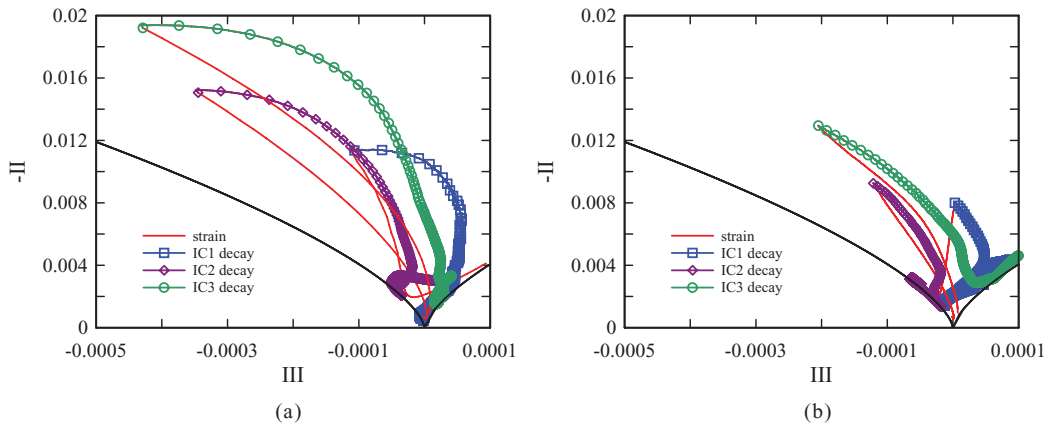

FIG. 11. Invariant plots Reynolds-stress anisotropy: (a) IC1: $Sk_0/\varepsilon_0 = 3.52$, IC2: $Sk_0/\varepsilon_0 = 3.46$, and IC3: $Sk_0/\varepsilon_0 = 3.37$; (b) IC1: $Sk_0/\varepsilon_0 = 0.352$, IC2: $Sk_0/\varepsilon_0 = 0.346$, and IC3: $Sk_0/\varepsilon_0 = 0.337$. The lowest black curves bound the realm of realizability. Solid red lines show the trajectory during the straining process and lines with symbols show the anisotropic decay trajectories.

strain proceeds, so that the following recovery (to isotropic structure) is much weaker on removal of the strain.

On this invariant map the classic linear return-to-isotropy model of Rotta[13] would be trajectories that only move downwards, never to the right. Those trajectories never overlap. More complicated nonlinear return-to-isotropy models, such as that of Sarkar and Speziale[42] do show trajectories that move to the right. However, those trajectories can still never cross each other. In Figure 11(a) there are a large number of trajectory crossings (for the different initial conditions). Trajectory crossing confirms the hypothesis that the time evolution of the anisotropy depends on more than just the anisotropy state itself.

F. Higher total strain

Figure 12 shows the effects of doubling the total strain for IC3 subjected to an initial strain-rate of $Sk_0/\varepsilon_0 = 0.337$, 0.843, and 1.686. Both the original strain of $ST = 0.5$ and doubled strain of $ST = 1.0$ are shown on each figure.

It can be seen that increasing the strain time increases the amount of anisotropy produced by the straining. In addition, it appears that the recovery slope depends on the strain-rate, and not the total strain. In fact, the low strain case (Figure 12(a)) appears to be recovering (moving to the right) even as the turbulence is strained. The faster the strain-rate, the smaller the strain time and the less recovery can happen during the straining process, and the more it happens after the strain is removed.

Note that all the doubly strained curves (upper blue curves) tend to move away from isotropy at very long times. This is probably because the mesh is no longer uniform at the end of the doubly

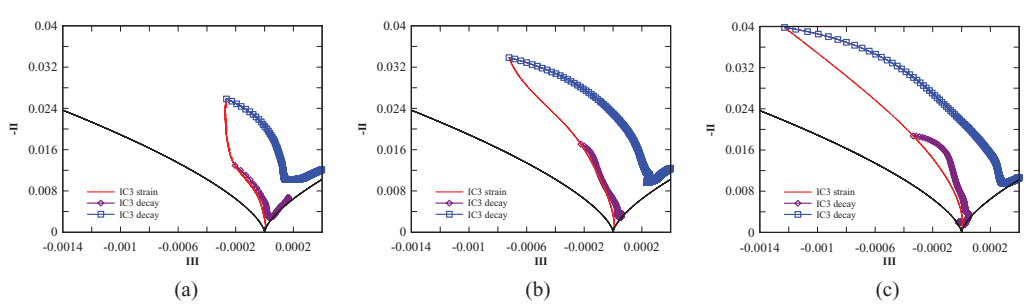

FIG. 12. Effect of doubling the strain time on IC3 for strain rates: $Sk_0/\varepsilon_0 =$ (a) 0.337, (b) 0.843, and (c) 1.686.

strained simulation cases. The mesh is, in fact, the reverse of the initial condition mesh before the straining. Differences in resolution in the three mesh directions may then cause slightly different decay rates in the three directions moving the turbulence away from isotropy at very long times. The very long time behavior of these doubly strained cases is therefore less accurate.

G. Decay rate

The decay rate is an extremely sensitive indicator of whether the turbulence is decaying like isotropic turbulence. The velocity derivative skewness, which is a more commonly used indicator, will stay at the classic value of −0.5 for all sorts of conditions where the decay rate shows a strong variation from the theoretical values. Figure 13 shows the decay rate n as a function of time for three different initial conditions and two different strain rates. The decay rate is given by $n^{-1} = \frac{d(K/\varepsilon)}{dt}$. It represents the power at which the kinetic energy decays, $(t) = K_0(t - t_0)^{-n}$. The numerical calculation of this quantity requires small time increments for an accurate representation of the derivative.[21] Before the strain is applied at time 12 the turbulence usually approaches the theoretically expected high Reynolds number value of 6/5 determined by Saffman.[43] Reference 27 shows this initial development behavior before this time but this work focuses on the strain and subsequent recovery. After the strain, the decay rate appears to approach the low Reynolds number Saffman theoretical value of 3/2. Then after more time, the higher Reynolds number cases (IC1 and IC2, see Figure 5) drop back towards the high Re decay rate, before finally moving towards the domain constrained decay exponent value of 2 (see Stalp *et al.*[44] and Touil *et al.*[45]) at very long times (after about 100 s). The highest Re case (IC2, at time 40) drops all the way to the high Re value. The medium Re case (IC1) only drops slightly, but does not go to 6/5. In any case, Ref. 21 looked at Re effects for decaying turbulence in more detail and showed that the decay rate transition from 6/5 to 3/2 is not solely related to the Reynolds number.

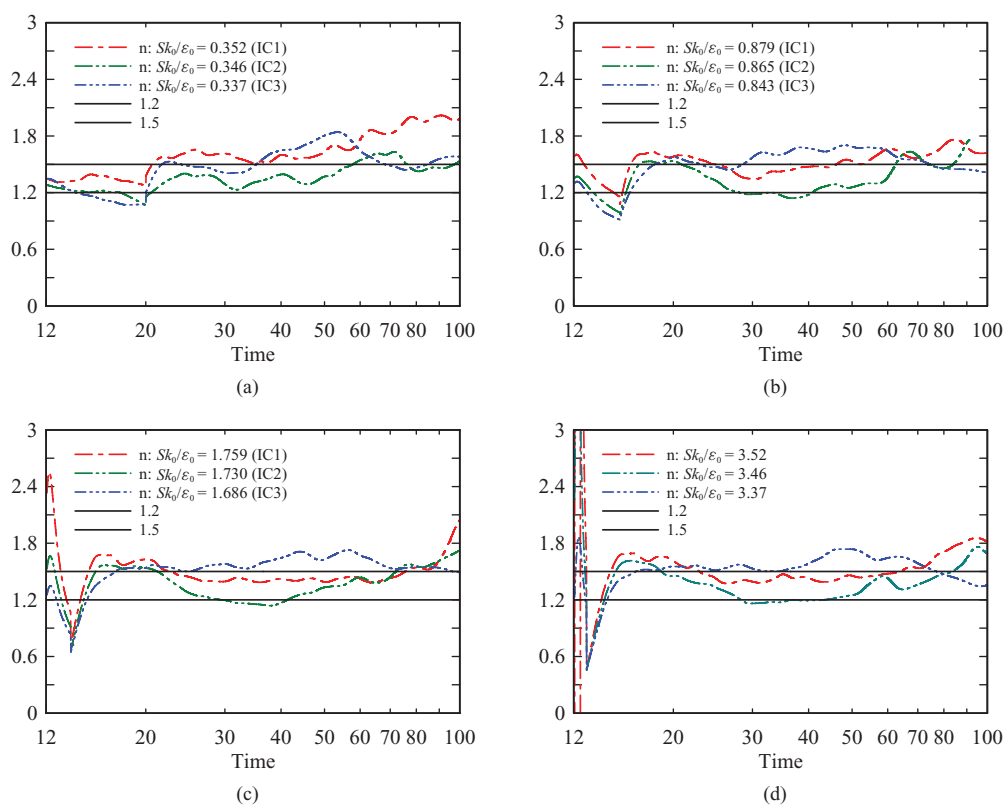

FIG. 13. Decay exponent, n, resulting from initial conditions IC1, IC2, and IC3 subjected to plane strain. $Sk_0/\varepsilon_0 \approx$ (a) 0.346, (b) 0.865, (c) 1.730, and (d) 3.46.

IV. MODELING

A. Anisotropy based models

Traditional return-to-isotropy models such as the linear Rotta,[13] or the more general nonlinear models (such as Sankar and Speziale[42]), attempt to characterize the return-to-isotropy using only the anisotropy tensor itself. A typical model is $\prod_{ij}/K = -(C_1 - 1)\frac{\varepsilon}{K}a_{ij} + C_n\frac{\varepsilon}{K}a_{ik}a_{kj}$, where $\prod_{ij}$ models the slow part of the pressure-velocity gradient correlation and the dissipation anisotropy. Note that C_1 should be greater than 1 or this model does not cause return to isotropy.

In the case of plane strain the anisotropy tensor has two independent quantities because the off diagonal components are zero and the diagonal components sum to zero. It is therefore possible to determine the two constants C_1 and C_n from the two independent anisotropy components $a_{11}(t)$ and $a_{22}(t)$, and their evolution in time (see Durbin and Reif[46] for more details). The values for these constants are shown in Figure 14 for the highest strain rate and three different initial conditions.

The analysis only applies after the strain stops (after 12.8 s). The general behavior of the constants is the same for the different initial conditions, but it is important to note that the constants change with time. There is an initial period where the linear return term (red solid line) is not causing return (C = 1) and the nonlinear term (blue dashed line) is doing all the return. Then at long times, the classic linear return model (with a value of about 1.7) seems to work very well.

Figure 15 shows the return constants for the IC3 case after a variety of different strain rates. The conclusions remain the same. At early times, something complex is happening, and the nonlinear model with a time varying constant is doing its best to capture the recovery (not return) of the turbulence. At latter times, the simple linear Rotta return model works very well.

It is possible, that the constants in the models above are actually a function of the anisotropy invariants (II and III) or other dimensionless variables such as the Re. References 14 and 15 contain examples of models where such functions have been hypothesized. Note, that no matter how complex the functional dependence of the model constants, a return-to-isotropy model that only depends on information contained in the anisotropy tensor produces unique trajectories on the invariant map that never cross (one state can never produce two different evolution paths for these models). The

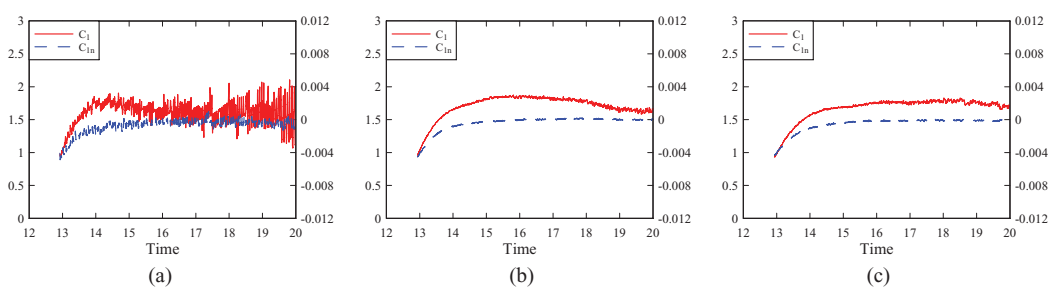

FIG. 14. Linear return to isotropy constant C_1 (solid red curve, left axis) and the nonlinear constant C_n (dashed blue curve, right axis) as a function of varying ICs (a) IC1 ($Sk_0/\varepsilon_0 = 3.52$), (b) IC2 ($Sk_0/\varepsilon_0 = 3.46$), and (c) IC3 ($Sk_0/\varepsilon_0 = 3.37$).

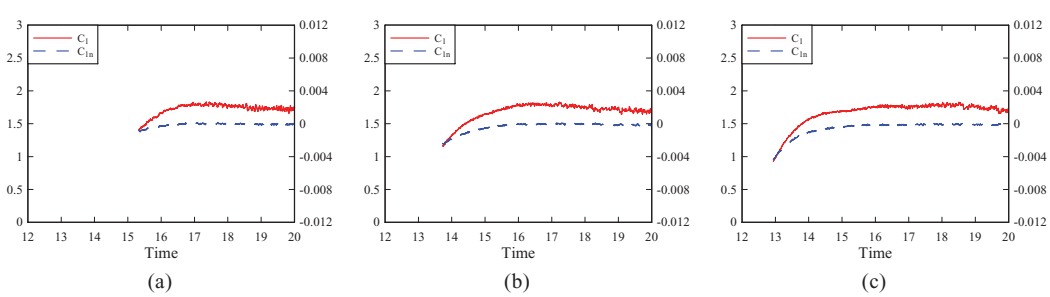

FIG. 15. Linear return to isotropy constant C_1 (solid red curve, left axis) and the nonlinear constant C_n (dashed blue curve, right axis) as a function of varying strain on IC3 (a) $Sk_0/\varepsilon_0 = 0.843$, (b) $Sk_0/\varepsilon_0 = 1.69$, and (c) $Sk_0/\varepsilon_0 = 3.37$.

crossings in Figure 11 suggest that additional information must be used in the return-to-isotropy model. The Reynolds numbers in these test cases do not vary significantly between initial conditions, or between the different strain rate tests, so it unlikely (in these simulations) to be the critical missing information. Section IV B considers the performance of a model which can account for eddy structure.

B. Oriented-eddy collision model

The oriented eddy collision (OEC) model is discussed extensively in Ref. 1. This model looks like a collection of Reynolds stress transport equations coupled with a set of transport equations for the inverse two-point correlation lengths. The information contained in the OEC model can be used to approximate the two-point correlation (not just its peak value which is the Reynolds stresses). In the OEC model the two-point correlation is approximated by $Q_{ij}(\mathbf{x}, \mathbf{r}) = \sum \hat{R}_{ij}(\mathbf{x}, t) f(|\mathbf{q}(\mathbf{x}, t) \cdot \mathbf{r}|)$, where $\hat{R}_{ij}(\mathbf{x}, t)$ and $\mathbf{q}(\mathbf{x}, t)$ are determined by the model partial differential equations (PDEs) and the function f is usually chosen to be a decaying exponential. The OEC model uses a classic linear return-to-isotropy model for the velocity fluctuations, and also the simplest possible linear return-to-isotropy model for the inverse correlation lengths, $\mathbf{q}$. However, the time scale for the $\mathbf{q}$-recovery is faster than that for the velocity-return.

The ability of the OEC model to predict the plane strain return is shown in Figure 16. This figure shows the Reynolds stresses for IC1 after 4 different strain rates. The OEC model is exact in the RDT limit, so the ability to capture the effect of straining which is normally quite difficult for turbulence models is not a problem for this model. The subsequent anisotropic decay (return-to-isotropy) is not exact for the OEC model. But the model uses the same information used to exactly predict the strain process, to also model the recovery process. The agreement over all 4 test cases (with the same model constants) is encouraging.

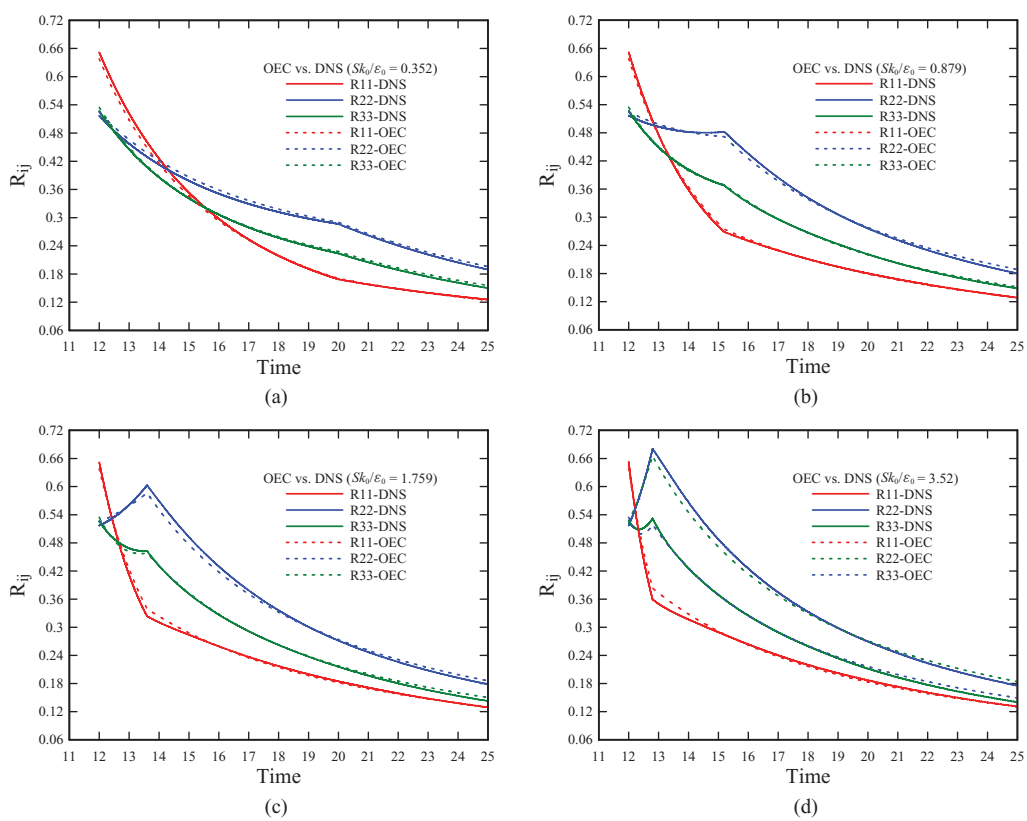

FIG. 16. Reynolds stresses for IC1 with DNS data (solid lines) and the OEC model (C_R 0.5 and C_L 0.67) predictions (dashed lines), for $Sk_0/\varepsilon_0 =$ (a) 0.352, (b) 0.879, (c) 1.759, and (d) 3.52.

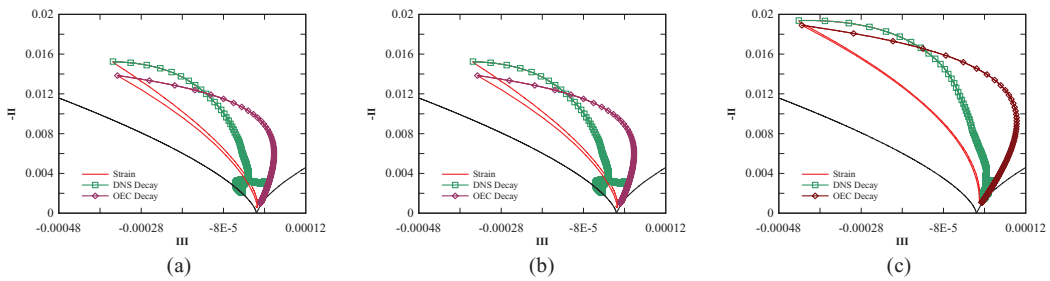

FIG. 17. DNS and OEC model predictions for the three different initial conditions at the highest strain rate. (a) IC1, $Sk_0/\varepsilon_0 = 3.52$, (b) IC2, $Sk_0/\varepsilon_0 = 3.46$, and (c) IC3, $Sk_0/\varepsilon_0 = 3.37$. The DNS is squares and the model is the diamonds.

A more sensitive test of the OEC model is to plot the results on the anisotropy invariant map. This is shown in Figure 17. The model produces the correct qualitative features. However, it tends to overshoot the recovery and move too far to the right on the invariant map. Note that this model can produce trajectory crossing like the DNS data demonstrates.

V. DISCUSSION

The simulations presented in this work have a 512^3 mesh resolution in order to try to capture the large scales well. Results suggest that the large-eddy length scale should be less than 1/4 of the domain size to prevent the turbulence from becoming domain constrained. The large scales are known from theory to govern the behavior of isotropic decay. They also appear to strongly influence the behavior of anisotropic turbulence. In particular, at long times we do not see a return-to-isotropy, but a return of the small scales to anisotropy and fixed background level of the large scale anisotropy. Comte-Bellot and Corrsin[30] make the same observations in their experiments as do Kang *et al.*[47] George[48] provides a possible theoretical argument for this behavior.

The initial conditions for the presented simulations were generated by moderate size cubes in a way that all large scales were formed by the turbulence process itself. The very largest scales of the turbulence (which govern the decay behavior) are much larger than the initial mixing cube size. There is very little human input to the simulation that influences the large scale turbulence. The very largest scales result from the Navier-Stokes equations and their interaction with a random arrangement of small cubes.

Because the large scales are much smaller than the domain size in these simulations, the turbulent Reynolds numbers are not large. Still, they are comparable to some experimental Reynolds numbers, and they appear to be high enough (at least for IC2) to produce the isotropic decay rate (n = 6/5) predicted by Saffman for high Re turbulent decay both before and well after the straining process. It was found that after straining, the turbulent decay rate tends to be larger than the theoretical value that one would expect for isotropic decaying turbulence (during the recovery phase). At longer times after the strain, the decay rate returns to its classic theoretically expected value even though the turbulence is not yet fully isotropic (during the return phase).

An important observation of this paper is the confirmation that the return-to-isotropy occurs in two stages, a **recovery** stage immediately after the strain is removed in which some of the anisotropy components can still be increasing (and the decay rate differs from its isotropic value), and after some time the more classic **return** stage where the velocity fluctuation anisotropy tends to zero (and the classic isotropic decay rates are applicable). We hypothesize that the recovery stage is the turbulence structure (two-point correlation lengths) returning to isotropy at a faster rate than the velocity fluctuations return (which is the classic return stage). The presence of crossing trajectories on the invariant map is a critical observation because it demonstrates unequivocally that the evolution of anisotropic turbulence cannot be captured by the information in the anisotropy tensor alone.

Classic models for return-to-isotropy process have been stymied because they did not account for the presence of the recovery stage of anisotropic turbulent decay. It was shown that even for

the same flow conditions, that different initial conditions produced quite different values for the constants in the classic nonlinear return to isotropy models.

Like the OEC model, the models of Kassinos, Reynolds, and co-workers[4,5] can also predict the two stages of anisotropic decay, recovery and return. However, the underlying models are related but not the same because of the difference in what type of extra information is being included in the model. Rather than the direct use of two-point information, Ref. 4 uses one-point correlations of derivatives while Ref. 5 makes use of a reduced spectral representation. The modeling of the results of Kassinos and Reynolds and the current DNS work both indicate that the recovery stage of anisotropic decay requires knowledge of and some representation of the turbulent structure.

This work only examines one type of anisotropic turbulence (plane strain), but it is encouraging that the OEC model gives fairly reasonably predictions for all the different initial conditions and strain rates with a single set of constants. Simulation and modeling of other canonical turbulent flows are ongoing.

ACKNOWLEDGMENTS

The bulk of these calculations were performed using NSF XSEDE supercomputing resources (Ranger) provided by the Texas Advanced Computing Center at the University of Texas at Austin. The work was supported in part by the Department of Energy via a subcontract from Oak Ridge National Laboratory, and primarily by the National Science Foundation (CBET Grant No. 1032364).

[1] M. B. Martell and J. B. Perot, "The oriented-eddy collision turbulence model," Flow, Turbul. Combust. **89**(3), 335 (2012).
[2] S. C. Kassinos and W. C. Reynolds, "A structure-based model for the rapid distortion of homogeneous turbulence," TF Report 61 (Thermosciences Division, Department of Mechanical Engineering, Stanford University, 1994).
[3] S. C. Kassinos, W. C. Reynolds, and M. M. Rogers, "One-point turbulence structure tensors," J. Fluid Mech. **428**, 213–248 (2001).
[4] S. C. Kassinos, C. A. Langer, S. L. Haire, and W. C. Reynolds, "Structure-based turbulence modeling for wall-bounded flows," Int. J. Heat Fluid Flow **21**, 599–605 (2000).
[5] S. C. Kassinos and E. Akylas, *New approaches in modeling multiphase flows and dispersion in turbulence, Fractal Methods and Synthetic Turbulence*, ERCOFTAC Series (Springer, 2012), Vol. 18, pp. 81–101.
[6] D. C. Besnard, F. H. Harlow, R. M. Rauenzahn, and C. Zemach, "Spectral transport model for turbulence," Los Alamos Report, LA-11821-MS, 1990.
[7] D. C. Besnard, F. H. Harlow, R. M. Rauenzahn, and C. Zemach, "Spectral transport model for turbulence," Theor. Comput. Fluid Dyn. **8**, 1–35 (1996).
[8] A. A. Townsend, "The uniform distortion of homogeneous turbulence," Q. J. Mech. Appl. Math. **7**, 104 (1954).
[9] H. J. Tucker and A. J. Reynolds, "The distortion of turbulence by irrotational plane strain," J. Fluid Mech. **32**, 657 (1968).
[10] A. J. Reynolds and H. J. Tucker, "The distortion of turbulence by general uniform irrotational strain," J. Fluid Mech. **68**(04), 657–673 (1975).
[11] J. N. Gence and J. Mathieu, "The return to isotropy of an homogeneous turbulence having been submitted to two successive plane strains," J. Fluid Mech. **101**, 555 (1980).
[12] L. Le Penven, J. N. Gence, and G. Comte-Bellot, "On the approach to isotropy of homogeneous turbulence: Effect of the partition of kinetic energy among the velocity components," Front. Fluid Mech. **1985**, 1 (A Collection of Research Papers Written in Commemoration of the 65th Birthday of Stanley Corrsin).
[13] J. C. Rotta, "Statistische theorie nichthomogener turbulenz,"Mitt. Z. Phys. **129**, 547 (1951).
[14] K. S. Choi and J. L. Lumley, "Turbulence and chaotic phenomena in fluids," in *Proceedings of the IUTAM Symposium, Kyoto, Japan*, edited by T. Tatsumi (North-Holland, Amsterdam, 1984), p. 267.
[15] J. L. Lumley and G. R. Newman, "The return to isotropy of homogeneous turbulence," J. Fluid Mech. **82**, 161 (1977).
[16] D. Kwak, W. C. Reynolds, and J. H. Ferziger, "Three-dimensional time dependent computation of turbulent flow," NASA Report TF-5 (1975), p. 1.
[17] R. S. Rogallo, "Numerical experiments in homogeneous turbulence," NASA Technical Memorandum 81315, 1981.
[18] M. J. Lee and W. C. Reynolds, "Numerical experiments on the structure of homogeneous turbulence," Report No. TF-24 (Department of Mechanical Engineering, Stanford University, 1985).
[19] M. M. Rogers and P. Moin, "The structure of vorticity fields in homogeneous turbulent flows," J. Fluid Mech. **176**, 33–66 (1987).
[20] C. Barre, F. Mashayek, and D. B. Taulbee, "Statistics in particle-laden plane strain turbulence by direct numerical simulation," Int. J. Multiphase Flow **27**(2), 347 (2001).
[21] N. K. R. Kevlahan and J. C. R. Hunt, "Nonlinear interactions in turbulence with strong irrotational straining," J. Fluid Mech. **337**, 333 (1997).
[22] G. K. Batchelor and I. Proudman, "The effect of rapid distortion of a fluid in turbulent motion," J. Mech. and Appl. Math. **7**(Pt. 1), 83 (1954).
[23] M. Hallbäck, J. Groth, and A. V. Johansson, "An algebraic model for nonisotropic turbulent dissipation rate in Reynolds stress closures," Phys. Fluids **2**(10), 1859 (1990).

[24] P. Moin and J. Kim, "Tackling turbulence with supercomputers," Sci. Am. **276**(1), 62–68 (1997).
[25] J. B. Perot and P. Moin, "Shear-free turbulent boundary layers, Part I: Physical insights into near wall turbulence," J. Fluid Mech. **295**, 199 (1995).
[26] J. B. Perot and P. Moin, "Shear-free turbulent boundary layers, Part II: New concepts for Reynolds stress transport equation modelling of inhomogeneous flows," J. Fluid Mech. **295**, 229–245 (1995).
[27] J. B. Perot, "Determination of the decay exponent in mechanically stirred isotropic turbulence," AIP Adv. **1**, 022104 (2011)
[28] P. G. Saffman, "The large-scale structure of homogeneous turbulence," J. Fluid Mech. **27**, 581 (1967).
[29] S. M. de Bruyn Kops and J. J. Riley, "Direct numerical simulation of laboratory experiments in isotropic turbulence," Phys. Fluids **10**, 2125 (1998).
[30] G. Comte-Bellot and S. Corrsin, "Simple Eularian time correlations of full and narrow-band velocity signals in grid generated isotropic turbulence," J. Fluid Mech. **48**, 273 (1971).
[31] T. Kurian and J. H. M. Fransson, "Grid-generated turbulence revisited," Fluid Dyn. Res. **41**(2), 021403 (2009).
[32] F. H. Harlow and J. E. Welch, "Numerical calculation of time-dependent viscous incompressible flow of fluid with free surface," Phys. Fluids **8**(12), 2182 (1965).
[33] J. B. Perot, "An analysis of the fractional step method," J. Comput. Phys. **108**(1), 51–58 (1993).
[34] W. Chang, F. Giraldo, and J. B. Perot, "Analysis of an exact fractional step method," J. Comput. Phys. **179**, 1–17 (2002).
[35] H. Le, P. Moin, and J. Kim, "Direct numerical simulation of turbulent flow over a backward step," J. Fluid Mech. **330**, 349 (1997).
[36] M. Martell, J. B. Perot, and J. Rothstein, "Direct numerical simulation of turbulent flow over drag-reducing ultrahydrophobic surfaces," J. Fluid Mech. **620**, 31 (2009).
[37] J. B. Perot, "Conservation properties of unstructured staggered mesh schemes," J. Comput. Phys. **159**(1), 58, (2000).
[38] J. B. Perot and V. Subramanian, "Discrete calculus methods for diffusion," J. Comput. Phys. **224**(1), 59 (2007).
[39] A. Wray, "Decaying isotropic turbulence," AGARD Advisory Report AR-345 (AGARD, 1998), p. 63.
[40] K.-S. Choi, "A study of the return to isotropy of homogeneous turbulence," *Sibley School of Mechanical and Aerospace Engineering* (Cornell University, 1983).
[41] J. L. Lumley, "Computational modeling of turbulent flows," Adv. Appl. Mech. **18**, 123–176, (1979).
[42] S. Sarkar and C. G. Speziale, "A simple nonlinear model for the return to isotropy in turbulence," Phys. Fluids A **2**, 84 (1990).
[43] P. G. Saffman, "Note on decay of homogeneous turbulence," Phys. Fluids **10**, 1349 (1967).
[44] S. R. Stalp, L. Skrbek, and R. J. Donnelly, "Decay of grid turbulence in a finite channel," Phys. Rev. Lett. **82**(24), 4831 (1999).
[45] H. Touil, J.-P. Bertoglio, and L. Shao, "The decay of turbulence in a bounded domain," J. Turbul. **3**, N49 (2002).
[46] P. A. Durbin and B. A. Pettersson Reif, *Statistical Theory and Modeling for Turbulent Flows*, 1st ed. (Wiley, 2001), p. 150.
[47] H. S. Kang, S. Chester, and C. Meneveau, "Decaying turbulence in an active-grid-generated flow and comparisons with large-eddy simulation," J. Fluid Mech. **480**, 129–160 (2003).
[48] W. K. George, "Asymptotic effect of initial and upstream conditions on turbulence," J. Fluids Eng. **134**, 061203 (2012).